Valence fluctuations in the 3D+3 modulated Yb3Co4Ge13 Remeika Phase

Feig, M.; Akselrud, L.; Motylenko, M.; Bobnar, M.; Wagler, J.; Kvashnina, K. O.; Rafaja, D.; Leithe-Jasper, A.; Gumeniuk, R.;

Originally published:

September 2021

Dalton Transactions 50(2021), 13580

DOI: https://doi.org/10.1039/D1DT01972D

Valence fluctuations in the $3D$+3 modulated $Yb_3Co_4Ge_{13}$ Remeika Phase

Manuel Feig,[†,‡] Lev Akselrud,[‡,¶] Mykhaylo Motylenko,[§] Matej Bobnar,[‡] Jörg Wagler,[‖] Kristina O. Kvashnina,[⊥,#] David Rafaja,[§] Andreas Leithe-Jasper,[‡] and Roman Gumeniuk[*,†,‡]

†*Institut für Experimentelle Physik, TU Bergakademie Freiberg, Leipziger Straße 23, 09596 Freiberg, Germany*

‡*Max-Planck-Institut für Chemische Physik fester Stoffe, Nöthnitzer Straße 40, 01187 Dresden, Germany*

¶*Ivan Franko National University of Lviv, Kyryla and Mefodiya Str. 6, UA-79005, Lviv, Ukraine*

§*Institut für Werkstoffwissenschaft, TU Bergakademie Freiberg, Gustav-Zeuner-Straße 5, 09599 Freiberg, Germany*

‖*Institut für Anorganische Chemie, TU Bergakademie Freiberg, Leipziger Straße 29, 09599 Freiberg, Germany*

⊥*European Synchrotron Radiation Facility, 71, Avenue des martyrs, Cedex 9, 38043 Grenoble, France*

#*Helmholtz-Zentrum Dresden-Rossendorf (HZDR), Institute of Resource Ecology, P.O. Box 510119, 01314 Dresden, Germany*

E-mail: roman.gumeniuk@physik.tu-freiberg.de

Abstract

$Yb_3Co_4Ge_{13}$ is the first example of a Remeika phase with a $3D + 3$ [space group $P\bar{4}3n(a,0,0)000(0,a,0)000(0,0,a)000$; $a = 8.72328(1)$ Å, $Q_1 = Q_2 = Q_3 = 0.4974(2)$] modulated crystal structure. A slight shift of the composition towards higher Yb-content (*i.e.* $Yb_{3.2}Co_4Ge_{12.8}$) leads to the disappearance of the satellite reflections and stabilization of the disordered primitive cubic [space group $Pm\bar{3}n$, $a = 8.74072(2)$ Å] Remeika prototype structure. The stoichiometric structurally modulated germanide is a metal with hole-like charge carriers, where Yb-ions are in a temperature dependent intermediate valence state of $+2.60 - +2.66$ for the temperature range $85 - 293$ K. The valence fluctuations have been investigated by means of temperature dependent X-ray absorption spectroscopy, magnetic susceptibility and thermopower measurements.

Introduction

Intermetallic clathrates,[1,2] filled skutterudites[3] and some Remeika phases[4,5] belong to the group of so-called cage-compounds, where a positively charged cation (mainly alkali-, alkaline-earth, rare-earth- or actinide-atom) is incorporated in an enlarged void formed by a negatively charged framework of covalently bonded $p-$ and $d-$elements. If a cage-compound contains an rare-earth (R) ion, then the combination of different chemical bondings (*i.e.* covalent and ionic) together with competition between the Kondo effect and the Ruderman-Kittel-Kasuya-Yosida interaction frequently result in such intriguing phenomena as superconductivity, heavy fermion state, quantum criticality, intermediate valence (IV) state, non-Fermi-liquid behavior etc.

R metals like Ce, Sm, Eu and Yb frequently reveal a non-integer valence in intermetallic compounds.[6,7] Such a behavior is caused by $4f$-states being localized in close vicinity to the Fermi level E_F, which means that in case of their hybridization both charge and spin fluctuations can occur. Such an IV state assumes for instance Yb-atoms to spend some time in a non-magnetic (*i.e.* $4f^{14}$) and another fraction of time in a magnetic ($4f^{13}$) configuration,

respectively. To describe the dynamics of the valence fluctuations (VF) the interconfigurational fluctuation (ICF)[8] and Kondo[9–11] models are usually used. The ICF model assumes the valence to depend on the energy difference between two corresponding states and on a characteristic fluctuation temperature. This model frequently fails to describe the VF in intermetallics containing Ce and Yb, since these atoms reveal complicated crystal electric field (CEF) multiplets ($J = 5/2$ and $J = 7/2$, respectively) splitting (for instance the splitting energy between the $J = 7/2$ ground state and $J = 5/2$ excited state for Yb^{3+} is particularly large and amounts $\sim 1.3\,\mathrm{eV}$ in YbCuAl[12] and YbB_{12}[13]). Therefore, the Kondo model, which takes into account the impurity-mediated hopping of the electrons between various total angular momentum eigenstates around it and thus, consider the whole multiplet[9] is more appropriate for the description of VF.

$Yb_3Co_4Ge_{13}$ is a Remeika phase reported to crystallize with the primitive cubic $Yb_3Rh_4Sn_{13}$ prototype, where the $24k$ site occupied by Ge-atoms is split.[14] As it is typical for IV systems, it reveals also a maximum in the magnetic susceptibility $\chi(T)$[14,15] as well as temperature dependent X-ray absorption spectra (XAS).[14] Both studies[14,15] analyzed $\chi(T)$ within the ICF model. The spin-fluctuation temperature $T_{\mathrm{sf}} = 226\,\mathrm{K}$ obtained in[14] and the exchange energy $E_{\mathrm{ex}} = 770\,\mathrm{K}$ indicated the mean valence of Yb-atoms $\nu = 2.66$. This value was also further confirmed by the deconvolution of X-ray absorption spectroscopy (XAS) data.

Since cage-compounds can reveal low thermal conductivity $\kappa(T)$ (due to their fillers-dominated phonon dispersions) and good electrical conductivity (due to the covalently bonded framework) they show promising thermoelectric (TE) properties. Morozkin *et al.*[16] investigated the TE performance of $Yb_3Co_4Ge_{13}$ and its doped variants $Yb_{3-x}R_xCo_4Ge_{13}$ ($R = \mathrm{La, Ce}$). However, these Remeika phases were found to possess small Seebeck coefficients ($S \sim 10 - 20\,\mu\mathrm{V\ K^{-1}}$ at $\sim 250\,\mathrm{K}$) and high $\kappa(T) \sim 8 - 16\,\mathrm{W\,m^{-1}\,K^{-1}}$ thus, indicating negligibly small TE performance with $ZT \sim 10^{-3}$ at RT. This could indicate $Yb_3Co_4Ge_{13}$ to be not a cage compound in the classical sense and thus, points towards a structural model of one of the distorted variants of the $Yb_3Rh_4Sn_{13}$ prototype reported recently in numerous

publications.[5,17–20]

In this work we show $Yb_{3+x}Co_4Ge_{13-x}$ to possess a homogeneity range with important consequences for the concomitant crystal structures. Combining powder and single crystal X-ray diffraction with a high resolution transmission electron microscopy study we discovered that the stoichiometric 3:4:13 germanide crystallizes with a non-centrosymmetric $3D + 3$ modulated variant of the $Yb_3Rh_4Sn_{13}$ Remeika type of structure.[4] However, off-stoichiometric $Yb_{3.2}Co_4Ge_{12.8}$ crystallizes with the structurally disordered primitive cubic $Yb_3Rh_4Sn_{13}$ Remeika prototype. The VF in the modulated $Yb_3Co_4Ge_{13}$ are analyzed on the base of the Kondo model. We also report the low temperature electrical and thermal transport properties for this Remeika phase.

Experimental

Two samples with the chemical compositions $Yb_3Co_4Ge_{13}$ and $Yb_{3.2}Co_4Ge_{12.8}$ have been synthesized from Ytterbium-ingots (Ames, 99.95 wt.%), Cobalt-foil (Chempur, 99.9 wt.%) and semiconductor-grade Germanium (Chempur, 99.9999 wt.%) pieces in a high frequency furnace (Trump Hüttinger) at a temperature $T \approx 1400\,^{\circ}\mathrm{C}$ (weight losses around 1 % and 0.6 %, respectively). The obtained pieces were placed in Carbon crucibles, enclosed in tantalum tubes, sealed in evacuated quartz glass ampules and annealed at 850 °C for 1 week. All manipulations were performed in a glove box system under protective argon atmosphere [$p(H_2O)$, $p(O_2) < 1$ ppm].

The samples were characterized by powder X-ray diffraction (PXRD) on a Huber G670 Guinier camera ($CoK_{\alpha 1}$ radiation, $\lambda = 1.78897$ Å). Further high-resolution PXRD was performed at the ID22 beamline of the European Synchrotron Radiation Facility (ESRF) for the $Yb_{3.2}Co_4Ge_{12.8}$ sample. Single crystal diffraction (SCXRD, two-circle diffractometer Stoe IPDS-2T, MoK_α, $\lambda = 0.71073$ Å) was performed on the mechanically extracted from the bulk sample crystals of ∼10–100 μm size).The lattice parameter refinement by least-squares

fitting, the Rietveld refinement, as well as all data transformations and manipulations concerning modulation were performed with the WinCSD software package.[21]

Transmission electron microscopy was used to verify the crystal structure of the sample. The transmission electron microscope JEM-2200FS from Jeol, which is equipped with a field emission gun (200 kV acceleration voltage), Cs corrector in the illumination system, high-resolution objective lens (Cs = 0.5 mm), omega filter and highly sensitive 2K × 2K CCD camera, was used in the conventional (TEM) and raster mode (STEM). The high-resolution (HRTEM) images and selected-area electron diffraction (SAED) images were recorded in the TEM mode, while in the STEM mode the high-angle annular dark-field (HAADF) detector for the estimation of atomic arrangement was used. The results were verified using corresponding simulations. The sample for the examination was prepared from the synthesized bulk sample using the focused ion beam (FIB) technique. The simulations of the HRSTEM contrast were carried out by considering the specific parameters of the TEM JEM-2200FS using the program "MacTampas".[22]

To perform microstructural analyses small pieces of the samples were embedded in a conductive resin, grinded and then polished. The obtained surfaces were investigated using a light-optical microscope (Zeiss Axioplan 2) and a scanning electron microscope (Jeol JSM - 7800F). The chemical composition was analyzed by means of energy dispersive X-ray spectroscopy (EDXS) (Quantax 400 EDXS system, Bruker). The obtained compositions $Yb_{3.2(1)}Co_{4.1(1)}Ge_{12.5(2)}$ (for the stoichiometric sample) $Yb_{3.4(1)}Co_{4.1(1)}Ge_{12.7(2)}$ (for the off-stoichiometric one) nicely reproduce the expected trends in Yb:Ge ratios, despite some inaccuracies in the Yb- and Ge-contents. To clarify this point some additional WDX study using appropriate standards would be necessary.

The X-ray absorption spectra (XAS) near the Yb L_{III} edge of $Yb_3Co_4Ge_{13}$ together with the non-diluted reference compounds Yb_2O_3 (Sigma-Aldrich) were measured in transmission mode in temperature range $85 - 293$ K at ROBL BM20 beamline of ESRF. The emission energy was selected using the $\langle 331 \rangle$ reflection of five spherically bent Ge crystal analyzers

aligned at 87° Bragg angle. The spectra were recorded at a scattering angle of 90° in the horizontal plane. The intensity was normalized to the incident flux. A combined (incident convoluted with emitted) energy resolution of 0.8 eV was determined from the full width at half maximum of the elastic peak.

The magnetic susceptibility was measured in a SQUID magnetometer (MPMS XL-7, Quantum Design).

The transport properties were measured down to 1.9 K using the TTO- and heat capacity options of an commercial system (PPMS, Quantum Design).

Results and discussion

Crystal structure

The strongest reflections of the PXRD pattern of $Yb_3Co_4Ge_{13}$ could be indexed with the cubic unit cell parameter (UCP) ≈ 8.72 Å (Laue class $m3m$), which fulfilled the extinction conditions hhl: $2h + l = 2n$ (possible SGs $Pm\bar{3}n$ and $P\bar{4}3m$). Further attempts to refine the crystal structure assuming such a symmetry resulted in a model analogous with that of $Yb_{3.2}Co_4Ge_{12.8}$ (see below as well as Tab. S1). However, the large number of weak reflections, which approximately correspond to the doubling of UCP could not be neglected. Therefore in the next step the structural model of the $La_3Rh_4Sn_{13}$ type (SG $I4_132$, $a \approx 17.5$ Å)[17] was chosen to describe the $Yb_3Co_4Ge_{13}$ structure. The crystallographic details of the refinement assuming such a model are given in Tab. 1. The final values of the atomic coordinates and displacement parameters are collected in Tab. S1. However, despite the low reliability factors (Tab. 1) the differential XRD profile obtained from such a refinement (Fig. 1a) revealed a rather poor description (blue line in Fig. 1c) of the weak satellites. Therefore to verify the structural model of the $Yb_3Co_4Ge_{13}$ germanide an additional TEM investigation was performed.

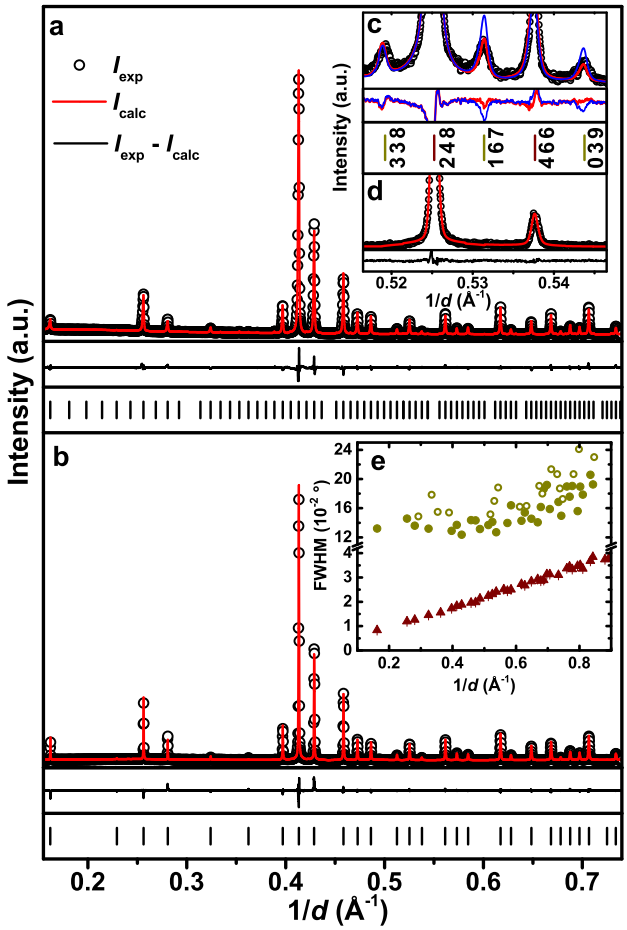

Figure 1: Powder X-ray diffraction (PXRD) patterns for $Yb_3Co_4Ge_{13}$ (SG $I4_132$) (a) and $Yb_{3.2}Co_4Ge_{12.8}$ (SG $Pm\bar{3}n$) (b). Inset c: selected $1/d$-range of the PXRD pattern of $Yb_3Co_4Ge_{13}$ (SG $I4_132$) together with the refinements assuming the $La_3Rh_4Sn_{13}$-model (blue line) and its split variant (red line) (see main text for more discussion). The indexing shows reflections simultaneous fulfilling a condition $h = 2n, k = 2n$ and $l = 2n$ (brown ticks) [coinciding nicely with the positions of (124) and (233) reflections for $Yb_{3.2}Co_4Ge_{12.8}$ (SG $Pm\bar{3}n$) (inset d)] as well as those corresponding exclusively to the SG $I4_132$ (*i. e.* breaking the above conditions) (dark yellow ticks). Inset e: full widths at the half maxima for both $Yb_3Co_4Ge_{13}$ (SG $I4_132$) (closed dark yellow circles for reflections simultaneously fulfilling condition $h = 2n, k = 2n$ and $l = 2n$ and open circles for those breaking it) as well as $Yb_{3.2}Co_4Ge_{12.8}$ (SG $Pm\bar{3}n$) (brown triangles).

Table 1: Crystallographic data for $Yb_{3+x}Co_4Ge_{13-x}$ ($x = 0, 0.2$)

Composition	$Yb_3Co_4Ge_{13}$	$Yb_3Co_4Ge^a_{13}$	$Yb_{3.2}Co_4Ge_{12.8}$
Space group (NN)	$P\bar{4}3n$ (a,0,0)000(0,a,0) 000(0,0,a)000	$I4_132$(214)	$Pm\bar{3}n$(223)
a (Å)	8.72328(1)	17.445(1)	8.7407(1)
$Q_1 = Q_2 = Q_3$	0.4974(2)		
Calculated density ρ (g cm^{-3})	8.45(1)	8.49(1)	8.56(1)
Detector	CCD	image plate	ID22 (ESRF)
Radiation, λ (Å)	Mo$K_{\alpha 1}$ 0.70930	Co$K_{\alpha 1}$ 1.78897	0.42768
Maximal $2\theta(^\circ)$	56.49	100	45
Minimum h, k, l	1, 0, -6	0, 0, 1	0, 0, 1
Maximum h, k, l	11, 8, 6	8, 10, 14	8, 11, 15
Minimum m_1, m_2, m_3	-1, -1, -1		
Maximum m_1, m_2, m_3	1, 1, 1		
$N(hkl)_{\text{measured}}$	18423		
Independent reflections	1902		
Main reflections	1210 ($R_\sigma = 0.0171$)		
Satellites	692 ($R_\sigma = 0.134$)		
Refined parameters	82	34	19
Goodness of fit, S	1.020		
R_{I}, R_{P}		0.054, 0.102	0.036, 0.066
R_{F}	0.0251		
R_{hkl000}	0.0495		
$R_{\text{hklm}_1\text{m}_2\text{m}_3}$	0.1688		
Residual peaks (e Å^{-3})	-0.94/1.23	-1.2/1.5	-2.7/3.3

[a] an averaged structure

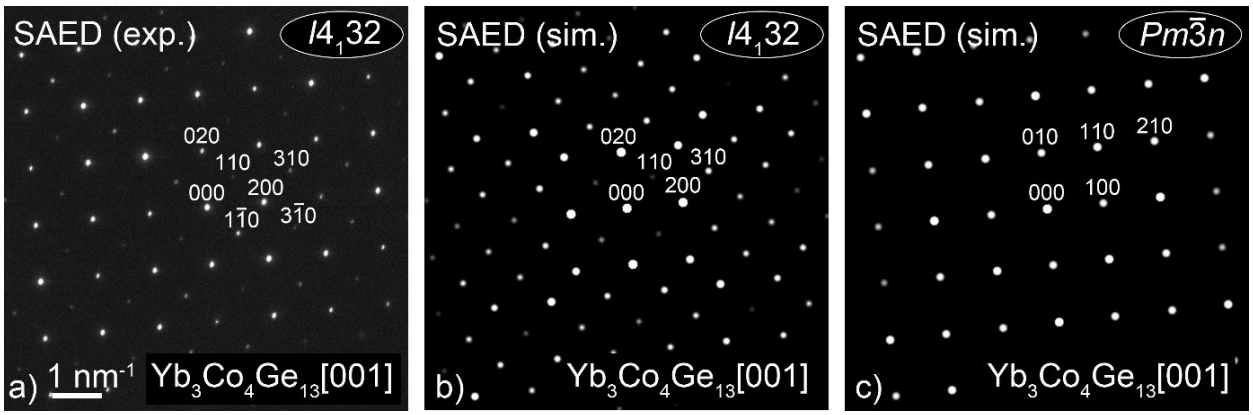

Figure 2: Comparison of measured and indexed SAED images of the $Yb_3Co_4Ge_{13}$ phase (a) with the calculated SAEDs of SG $I4_132$ (b) and SG $Pm\bar{3}n$ (c) for the zone axis [001].

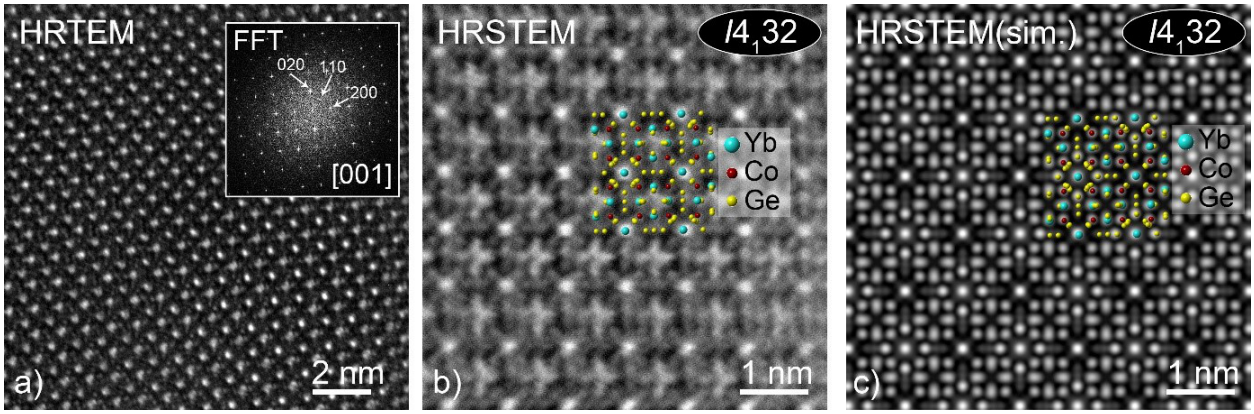

Figure 3: HRTEM image of a [001]-oriented $Yb_3Co_4Ge_{13}$ crystal (a) with corresponding indexed FFT (inset), measured (b) and simulated (c) HRSTEM DF image of the $I4_132$ phase with an overlay of the corresponding crystal lattice.

The phase analysis of the FIBed sample was carried out by means of electron diffraction in the TEM. The indexed SAED image (Fig. 2a) could be assigned to the SG $I4_132$. A comparison of two simulated SAED images (Fig. 2b,c) clearly show that the (110) and (310) reflections are only characteristic for the structural model within the SG $I4_132$. The simulation was carried out with the software JEMS[23] based on the principles of the dynamic theory of electron diffraction. For the simulations the experimental parameters of the microscope and the sample thicknesses of 139.5 nm and 123.9 nm for the $I4_132$ phase (Fig. 2b) and $Pm\bar{3}n$ phase (Fig. 2c) were used, respectively. The deviations between the intensities of the corresponding peaks in the measured (Fig. 2a) and simulated (Fig. 2b) SAED images are

due to dynamic effects.

The phase assignment was also carried out using high-resolution microscopy. For this purpose, the high-resolution contrasts were analyzed both by fast Fourier transform (FFT) and by comparing the experimental and simulated HR(S)TEM images (Fig. 3). As it was found in the SAED pattern, the FFT of HRTEM shows the presence of phase-specific reflections, *e.g.* (110) (inset to Fig. 3a) for the same [001]-orientation of the sample (Fig. 3a). Due to the strong dependence of the phase contrast of the HRTEM images on the defocus and sample thickness, it is difficult to compare the measured and simulated HRTEM images. It is much easier in the case of HRSTEM DF images. The recorded (Fig. 3b) and simulated (Fig. 3c) HRSTEM DF images show a good agreement with each other as well with the corresponding atomic arrangement of the $I4_132$ phase (*i.e.* $La_3Rh_4Sn_{13}$ type[17]) (overlays in Fig. 3b,c).

However, despite the fact that the PXRD and TEM data of $Yb_3Co_4Ge_{13}$ could be acceptably described with the non-centrosymmetric body-centred $La_3Rh_4Sn_{13}$ model, the former failed completely in the description of the single crystal XRD (SCXRD) data. The main problem was that the satellites indicating the doubling of UCP could be indexed only approximately. This discrepancy is already visible in the indexing of the PXRD data, where standard deviations for the majority of satellites (12 of 19 observed) are by a factor of ~ 2 larger than those of the main reflections (Fig. S1). Additionally, as one can see from Fig. 1e, the satellites are normally broader than the main reflections. These puzzling results indicated a possibly modulated crystal structure and prompted us to transform the diffraction peaks with the help of a 3-dimensional modulation vector [α 0 0] [0 α 0] [0 0 α] (where $\alpha \approx 0.5$) and re-index them now with 6 indexes $hklm_1m_2m_3$ characteristic for a $3D + 3$ modulated structure. In this notation $3D$ represents the dimension of the physical three-dimensional space (where e.g. the atoms are positioned) whereas 3 additional dimensions, orthogonal to $3D$, are necessary to describe the modulation.[24] Further, the UCP and the modulation vector α were precisely estimated from the indexing and Rietveld refinement of PXRD data

(Tab. 1).

The analysis of the extinction conditions [*i.e.* $hhlm_1m_1m_3$ with $l = 2n$, $h(-h)lm_1(-m_1)m_3$ with $l = 2n$, $hkhm_1m_2m_1$ with $k = 2n$, $hk(-h)m_1m_2(-m_1)$ with $k = 2n$, $hkkm_1m_2m_2$ with $h = 2n$ and $hk(-k)m_1m_2(-m_2)$ with $h = 2n$] indicated the superspace groups $Pm\bar{3}n(a,0,0)$ $000(0,a,0)000(0,0,a)000$ and $P\bar{4}3n(a,0,0)000(0,a,0)000(0,0,a)000$ in the notation after Stokes, Campbell and van Smaalen.[25,26] Further refinements revealed that a reasonable structural model could be found only adopting the non-centrosymmetric superspace group.

In the first step of the refinement, the basic structure in the $3D$ space group $P\bar{4}3n$ (*cf.* Tab. S1) was refined and then the satellites were added. In the subsequent step, positional and occupational modulations described by modulation functions (MF) of the first order (listed in supporting information) were applied. The intensities of higher orders at the respective estimated value of the modulation vector are not observable. Contrary to $3D + 1$ modulations, where positional MFs are simple *sin* or *cos* functions and occupational modulations are described by so-called crenel functions,[27] the $3D + 3$ modulation assumes the coordinates of the basic structure (*i.e.* x_0, y_0, z_0, see formulas in supporting information) to be additionally altered by complicated superpositions of sin or cos functions in super-space (*i.e.* coordinates x_4, x_5, x_6) in both cases. And even more, having parametrized the positional and occupational MFs it remains to consider their $3D$ "shape" in super-space (i.e. as functions of x_4, x_5, x_6) and the implied structural consequences of this "shape" for the real $3D$ physical space.[28] The real crystal can be understood as a three-dimensional section through the $(3D+3)$-dimensional periodic 'supercrystal' and the diffraction pattern of the modulated crystal is treated as the projection of its $(3D + 3)$-dimensional reciprocal lattice.[24,29]

The refined atomic coordinates for $Yb_3Co_4Ge_{13}$, modulation amplitudes of the positional modulations as well as the occupational modulation amplitudes for Ge-atoms at the split positions are collected in Tab. S1, Tab. S2 and Tab. S3, respectively. No modulation was applied for the refinement of the displacement parameters (Tab. S4).

The refined occupational MFs for Ge2- and Ge3-atoms are presented in $3D$ super-space

as dependence of x_4, x_5, x_6 in Fig. 4. As one can see, the maxima calculated from the refined parameters of the modulated occupancies for Ge3-atoms coincide with the minima of position occupancies for Ge2. Here it should be noted, that the powder Rietveld refinement (not presented in Tab. S1) results in practically full statistical distribution of Ge2 and Ge3 atoms. This might indicate the existence of disproportionate partial ordering in different crystallites, where different distributions of position occupancy functions occur.

In addition, the modulated structural model obtained from SCXRD was used to refine PXRD data. As it is clearly visible from Fig. 1c it provides a much better description of the satellites (red line) in comparison with those obtained from the non-centrosymmetric body-centred $La_3Rh_4Sn_{13}$ model (blue line). Providing an approximate description for both the powder- and single crystal XRD data the latter structural model could be considered as an averaged one for the complex modulated structure.

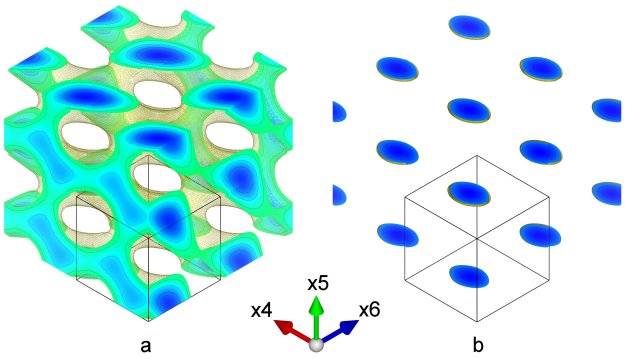

Figure 4: $3D$ positional MFs distribution dependence in the super-space (x_4, x_5, x_6 vary within $0 \div 2$) for Ge2 (a) and Ge3 (b) in the modulated $Yb_3Co_4Ge_{13}$ structure. The isosurfaces with occupancy $G = 0.64$ are shown.

The $Yb_{3.2}Co_4Ge_{12.8}$ sample was also characterized with high resolution PXRD (Fig. 1b). Interestingly, in this diffraction pattern no satellites are observed and the peaks reveal a very narrow FWHM (*i.e.* $0.01 - 0.03°$) (Fig. 1e). They can be indexed within the cubic primitive lattice with the UCP $a = 8.7407(1)$ Å (i.e. by a factor of ~ 2 smaller than the value of the lattice parameter of the stoichiometric $Yb_3Co_4Ge_{13}$ averaged structure) (Tab. 1). The close relationship between both UCPs is nicely seen in Figs. 1c and 1d: the *hkl* reflections with

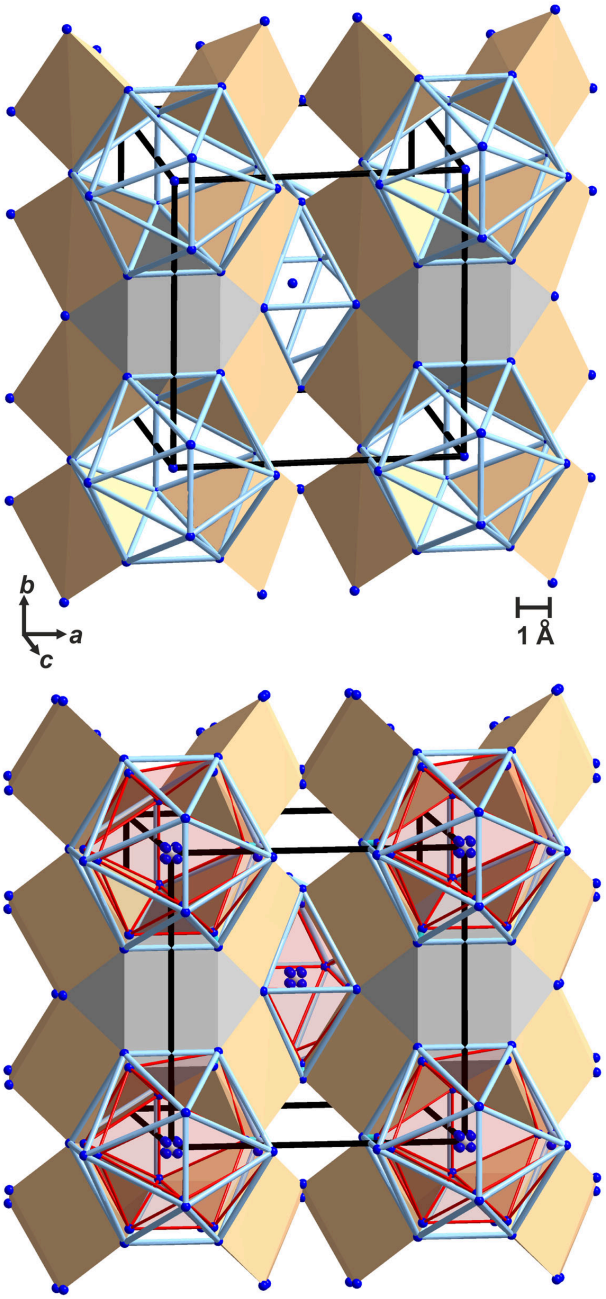

Figure 5: Array of the corner sharing [$RhGe_6$] trigonal prisms (tan) together with [$Ge1Ge_{12}$] or [$Yb2Ge_{12}$] icosahedra (pale blue) as well as [$Yb1Ge_{12}$] cuboctahedra (light grey) in the crystal structures of idealized $Yb_3Co_4Ge_{13}$ (*i.e.* $Yb_3Rh_4Sn_{13}$ prototype) (upper panel) and the off-stoichiometric $Yb_{3.2}Co_4Ge_{12.8}$ split variant (lower panel). Ge-atoms are shown as blue balls, whereas Yb-atoms are in grey. The 'doubled' vertices of all polyhedra (the red [$Yb2Ge_{12}$] icosahedra incorporated in the pale blue ones are shown to stress this situation) are not real because of the statistical occupancy of the Ge2- and Ge2a-sites (Tab. S1).

the condition $h = 2n, k = 2n$ and $l = 2n$ [in the case of SG $Pm\bar{3}n$ they correspond to indices $h/2$, $k/2$, $l/2$ (not shown in Fig. 1c)] are common for both powder patterns, while those breaking it are observed only for $Yb_3Co_4Ge_{13}$. However, the Rietveld refinement assuming the structural model of the fully ordered Remeika $Yb_3Rh_4Sn_{13}$ prototype[4] for $Yb_{3.2}Co_4Ge_{12.8}$ resulted in high values of the reliability factor ($R_I = 0.067$) and residual electron density (ED) of $11.2\,e\,Å^{-3}$. This density was localized near the position of the Ge2-atom and split of this crystallographic site led to $R_I = 0.057$ and ED of $8.8\,e\,Å^{-3}$. Further Fourier transformation indicated that this ED is now localized near the Ge1-atom. Its shift off the centre as well as the introduction of an additional Yb-atom partially occupying the $2a$ site brought us to the final values of R_I, residual peak in ED and atomic parameters presented in Tabs. 1 and S1, respectively. The strong structural disorder in $Yb_{3.2}Co_4Ge_{12.8}$ is in line with numerous similar reports for 3:4:13 Remeika phases (see Tab. 1 in[5] as well as[30,31]). We infer from these observations that the $Yb_3Co_4Ge_{13}$ samples investigated in[14] and[15] probably were slightly off-stoichiometric.

The close structural relationship within the group-subgroup scheme between Remeika phases crystallizing with $Yb_3Rh_4Sn_{13}$ (SG $Pm\bar{3}n$) and $La_3Rh_4Sn_{13}$ (SG $I4_132$) types is widely discussed in the literature.[5,18–20] Both structures are characterized by a corner sharing trigonal prismatic array with icosahedra and cuboctahedra in the space in-between. Such structural arrangements for idealized $Yb_3Co_4Ge_{13}$ (i.e. $Yb_3Rh_4Sn_{13}$ prototype) and the off-stoichiometric $Yb_{3.2}Co_4Ge_{12.8}$ split variant are presented in Fig. 5.

The interatomic distances in the stoichiometric $Yb_3Co_4Ge_{13}$ averaged structure as well as in $Yb_{3.2}Co_4Ge_{12.8}$ are collected in Tab. S5. They are characterized by no Yb-Yb and Co-Co bonding contacts. Ge-Ge distances are slightly larger than the sum of atomic radii of germanium ($r_{Ge} = 1.25\,Å$[32]). The shortenings of Yb-Ge, Yb-Co and Co-Ge contacts varies within $4.5 - 6.8\,\%$, $3.3 - 4.6\,\%$ and $4.0 - 9.3\,\%$, respectively. All these observations agree well with earlier reports for Remeika phases.[5,18,19]

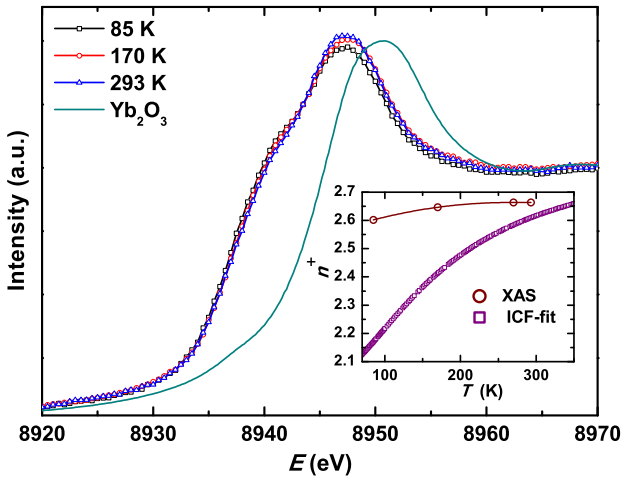

Figure 6: X-ray absorption spectra (XAS) of $Yb_3Co_4Ge_{13}$ at different temperatures together with the spectrum of Yb_2O_3 as a reference compound. Inset: temperature change of Yb valence deduced from the deconvolution of XAS as well as from the ICF model applied to the magnetic susceptibility (see text below).

X-ray absorption spectroscopy

Temperature dependent X-ray absorption spectra (XAS) of $Yb_3Co_4Ge_{13}$ in comparison with the Yb_2O_3 reference compound are depicted in Fig. 6. The measured XAS clearly reveal two white lines. The high-energy one (centred at $\sim$ 8947 eV) coincides almost with the absorption peak of Yb_2O_3 and thus, corresponds to an $4f^{13}$ (Yb^{3+}) configuration. The low energy shoulder near $\sim$ 8940 eV is due to the $4f^{14}$ (Yb^{2+}) state. As one can see from Fig. 6 the intensities of both white lines in the XAS of $Yb_3Co_4Ge_{13}$ are slightly temperature dependent (the intensity of the high-energy feature increases with increasing temperature, while those of the low-energy one decreases). All these observations indicate Yb-atoms displaying a temperature dependent intermediate valence in the structure of $Yb_3Co_4Ge_{13}$. The deconvolution of the measured spectra indicate a small valence change of $+2.60(1) - +2.66(1)$ in the temperature range $85-293$ K (inset to Fig. 6). This result is in fair agreement with the earlier reported $Yb^{+2.66(3)}$ valence at 77 K.[14]

Magnetic susceptibility

The magnetic susceptibilities $\chi(T)$ of $Yb_3Co_4Ge_{13}$ measured in this work as well as those measured in[14,15] are presented in Fig. 7a. They are almost identical for all three samples for $T > 50\,\mathrm{K}$, while for the lower temperature range $\chi(T)$ of the material investigated by Mudryk *et al.*[14] reveals a very strong upturn. This could be attributed to a higher content of paramagnetic impurity. This comparison shows also that the bulk sample synthesized in this work is of the comparable quality as the single crystal from Ref. [15] The similarity of $\chi(T)$ of the obviously off-stoichiometric samples (containing material with primitive cubic structures) analysed in[14] and[15] with the body-centred one investigated here confirm again the same cuboctahedral environment (*i.e.* $[YbGe_{12}]$) in both structures, as it is shown in Ref. [5]

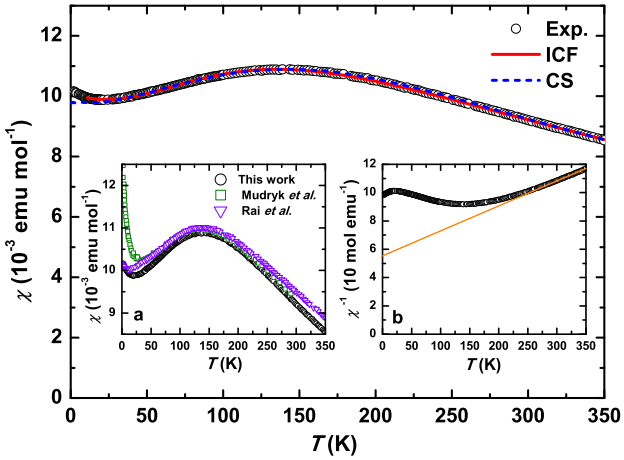

Figure 7: Temperature dependence of the magnetic susceptibility of $Yb_3Co_4Ge_{13}$ together with a fit to the ICF model and with the prediction of the Coqblin-Schrieffer (CS) model for $J = 5/2$ ($\chi_0 = 4.15 \times 10^{-2}$; $T_0 = 584\,\mathrm{K}$). Inset a: Magnetic susceptibility for $Yb_3Co_4Ge_{13}$ measured in this work in comparison with those reported by Mudryk *et al.*[14] and by Rai *et al.*.[15] Inset b: reciprocal magnetic susceptibility for $Yb_3Co_4Ge_{13}$ together with the Curie-Weiss fit (orange line).

The magnetic susceptibility of $Yb_3Co_4Ge_{13}$ fits to a Curie-Weiss (CW) law in the temperature range $240 - 400\,\mathrm{K}$ (Fig. 7b). The fit results in an effective magnetic moment $\mu_{\mathrm{eff}} = 4.1(1)\,\mu\mathrm{B}$ (close to the theoretically calculated Yb^{3+}-ion value of $4.54\,\mu\mathrm{B}$) and the high negative Weiss temperature $\Theta_{\mathrm{P}} = -382(3)\,\mathrm{K}$, which is due to the large characteristic

energy ($\sim 150\,\mathrm{K}$) of the valence fluctuations in the studied compound (see below).

Below $240\,\mathrm{K}$ $\chi(T)$ of $Yb_3Co_4Ge_{13}$ (Fig. 7) deviates drastically from the CW-like dependence, shows a maximum centred at $\sim 150\,\mathrm{K}$, then decreases down to $25\,\mathrm{K}$ and finally slightly increases below this temperature. This is a typical behaviour expected for systems with IV state of Yb atoms,[33,34] which is in agreement with the performed XAS measurements.

Firstly, we tried to analyze $\chi(T)$ of $Yb_3Co_4Ge_{13}$ by applying the interconfiguration fluctuation model (ICF).[8] The magnetic susceptibility within this model is given as:

$$\chi_{\mathrm{ICF}}(T) = N_{\mathrm{A}}\mu_{\mathrm{eff}}^2 \frac{1-\nu_{\mathrm{eff}}}{k_{\mathrm{B}}(T+T_{\mathrm{sf}})} \tag{1}$$

where ν_{eff} is the fractional occupation of the divalent state and it can be calculated from:

$$\nu_{\mathrm{eff}} = \frac{1}{1+8\exp[-E_{\mathrm{ex}}/k_{\mathrm{B}}(T+T_{\mathrm{sf}})]} \tag{2}$$

In the formula above, E_{ex} is the interconfigurational excitation energy and T_{sf} defines the width of all sublevels of the two configurations. Since the studied $Yb_3Co_4Ge_{13}$ sample shows some CW impurity contributions for $T < 25\,\mathrm{K}$ and paramagnetism due to conduction-electrons the $\chi_{\mathrm{imp}}(T) = C_{\mathrm{imp}}/(T-\Theta_{\mathrm{imp}})$ and χ_0, have to be used, respectively. Thus the $\chi(T)$ of $Yb_3Co_4Ge_{13}$ is described by:

$$\chi(T) = \chi_{\mathrm{ICF}}(T) + \chi_{\mathrm{imp}}(T) + \chi_0 \tag{3}$$

A fit to Eq. 3 is given in Fig. 7 by the blue dashed line and results in $E_{\mathrm{ex}}/k_{\mathrm{B}} = 613(2)\,\mathrm{K}$; $T_{\mathrm{sf}} = 82.7(4)\,\mathrm{K}$; $C_{\mathrm{imp}} = 4.5(2)\,\mathrm{emu\,K\,mol^{-1}}$; $\Theta_{\mathrm{imp}} = -396(9)\,\mathrm{K}$ and $\chi_0 = -1.4(1) \times 10^{-3}\,\mathrm{emu\,mol^{-1}}$ (values close to those published in Ref. [15]). The average valence of Yb atoms in $Yb_3Co_4Ge_{13}$ can be calculated as $n = 2\nu_{\mathrm{eff}} + 3(1-\nu_{\mathrm{eff}})$. As one can see from the inset to Fig. 6 the ICF valence values are much smaller, than those estimated from XAS. Close values of n, *i.e.* +2.61 (ICF) and +2.66 (XAS), are observed only for $T > 300\,\mathrm{K}$.

Valences calculated from magnetic susceptibility at lower temperatures decrease much stronger. This can be explained by a drastic decrease of the fractional occupancy ν_{eff} below 150 K, which follows the $\chi(T)$ dependence. The failure of the ICF model to describe the mean valence of R-atoms is known for some Ce-,[35,36] Eu-[37–39] and Yb-containing[40,41] IV systems.

A broad maximum in $\chi(T)$ is a characteristic feature of a Kondo system with large characteristic energy. As it is seen in Fig. 7 the Coqblin-Schrieffer (CS) model proposed by Rajan for the multiplet $J = 5/2$ and degeneracy $N = 6$[9] perfectly fits with the magnetic susceptibility of $Yb_3Co_4Ge_{13}$ in the temperature range $30 - 400$ K. The scaling energy $T_0 = 584$ K, obtained from adjustment of the Kondo model to our experiment, is converted into a Kondo temperature (in its high-T definition) according to $T_K = 2\pi T_0 W_J/(2J+1) = 396$ K, where $W_{5/2} = 0.6468$ is a Wilson number that relates χ_0 to T_K.[42]

Here it should be also noted that $\chi(T)$ of $Yb_3Co_4Ge_{13}$ rather has to be fitted including the whole Yb^{3+} muliplet $J = 7/2$ ($N = 8$). The failure of such a description is due to the fact that the CS-model does not take into account the crystal electric field (CEF) splitting effects.[9] Since in the $3D$+3 modulated structure of $Yb_3Co_4Ge_{13}$ the point symmetry of the Yb-position cannot be even described within a conventional crystallography (i.e. is low) the CEF splitting effects are expected to be of a very complex character. Similar situations, where the maxima in $\chi(T)$ were actually described by the lowered due to CEF effects) $J = 5/2$ multiplet are reported for e.g. YbCuAl[43] and $YbCu_{5-x}Ag_x$,[44] which are much simpler cases in comparison with $Yb_3Co_4Ge_{13}$ since they crystallize with the conventional hexagonal Fe_2P[45] and $CaCu_5$[46] structure types.

Transport properties

The low temperature specific heat of $Yb_3Co_4Ge_{13}$ (Fig. 8) reveals field dependent λ-anomalies below 3 K (inset to Fig. 8). The anomaly in 0-field is centred at ~ 2.3 K, which would correspond to the antiferromagnetic ordering (AFO) of Yb_2O_3.[47] Since no signs of any AFO

are visible in the magnetic measurements and no peaks belonging to Yb_2O_3 are detected in the HR XRD pattern we have to conclude that the oxide impurity in $Yb_3Co_4Ge_{13}$ is of minor character and < 0.5 mol. %.

In the temperature range $3-11$ K the c_p/T (T^2) dependence for $Yb_3Co_4Ge_{13}$ is linear and has been fit to the $c_p = \gamma T + \beta T^3$ ansatz. From the fit we find: $\gamma = 105.0(5)\,\mathrm{mJ\,mol^{-1}\,K^{-2}}$ and $\beta = 4.08(9)\,\mathrm{mJ\,mol^{-1}\,K^{-4}}$ indicating a Debye temperature $\Theta_\mathrm{D} = 212(1)$ K.

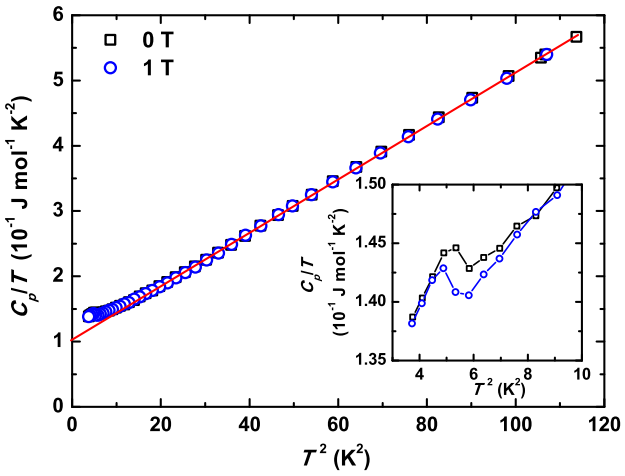

Figure 8: Specific heat of $Yb_3Co_4Ge_{13}$ in c_p/T vs T^2 presentation together with the fit to $c_\mathrm{p} = \gamma T + \beta T^3$ ansatz (red line). Inset: field dependent anomalies due to antiferromagnetic ordering of an Yb_2O_3 impurity.

The temperature dependence of electrical resistivity $\rho(T)$ for $Yb_3Co_4Ge_{13}$ is depicted in Fig. 9. It increases with increasing temperature in the whole studied temperature range and is of the same order of magnitude as expected for a metal. The residual resistance ratio (RRR), defined as $\rho_{300}/\rho_0 = 1.55$, is rather small and indicates a high concentration of defects (which could be related to the complicated modulated crystal structure) in the investigated sample. For $2\,\mathrm{K} < T < 125\,\mathrm{K}$ $\rho(T)$ for $Yb_3Co_4Ge_{13}$ fits nicely to $\rho_0 + A_\mathrm{FL}T^2$ with the residual resistivity $\rho_0 = 2.26(1)\,\mu\Omega\,\mathrm{m}$ and cross section of the quasiparticle-quasiparticle scattering $A_\mathrm{FL} = 3.1(2) \times 10^{-3}\,\mu\Omega\,\mathrm{cm\,K^{-2}}$. Thus, the Kadowaki-Woods ratio[48] $R_\mathrm{KW} = A_\mathrm{FL}/\gamma^2 = 2.8 \times 10^{-7}\mu\Omega\,\mathrm{cm}\ (\mathrm{mol\,K\,mJ^{-1}})^2$ for $Yb_3Co_4Ge_{13}$ is very close to the value of $4 \times 10^{-7}\mu\Omega\,\mathrm{cm}\ (\mathrm{mol\,K\,mJ^{-1}})^2$ reported for Yb-based IV systems.[49]

The temperature dependence of the Seebeck coefficient of thermopower for $Yb_3Co_4Ge_{13}$

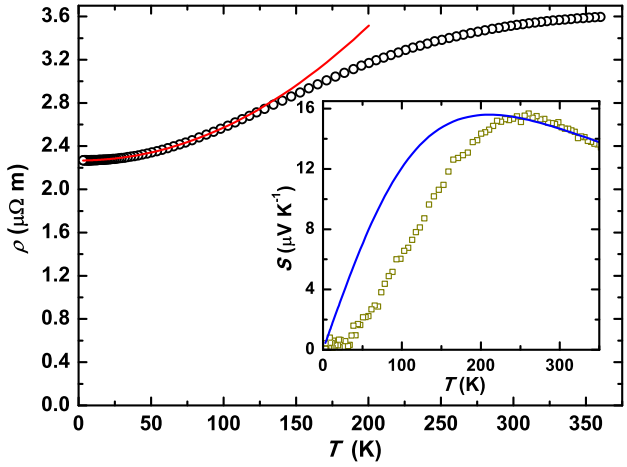

Figure 9: Temperature dependence of the electrical resistivity of $Yb_3Co_4Ge_{13}$ together with the fit to $\rho_0 + A_{FL}T^2$ (red line). Inset shows temperature dependence of the Seebeck coefficient of thermopower together with the fit to $S = AT/(B^2 + T^2)$.

is presented in the inset to Fig. 9. The small values of the thermopower and the linear increase of $S(T)$ in a wide temperature range (*i.e.* $30 - 200$ K) are typical features of a metal. The positive values of S indicate hole-like conductivity in $Yb_3Co_4Ge_{13}$. As expected for IV systems $S(T)$ shows also a broad and pronounced maximum centered at 250 K. Such a maximum can be described with $S = AT/(B^2 + T^2)$ within a phenomenological model for the quasiparticle electronic density of state (DOS), N^{4f} at the Fermi level.[50] The best fit to the formula above, which could be obtained for $S(T)$ of $Yb_3Co_4Ge_{13}$, resulted in $A = 6.6(1) \times 10^3\,\mu$V and $B = 4.4(1) \times 10^4\,$K^2. As one can see in the inset to Fig. 9 the phenomenological model provides only a very rough description of the thermopower. This again confirms a complex mechanism of the valence fluctuations in $Yb_3Co_4Ge_{13}$.

The thermal conductivity $\kappa(T)$ for $Yb_3Co_4Ge_{13}$ is shown in Fig. 10. It decreases smoothly with decreasing temperature from 350 K to 100 K. Below 100 K $\kappa(T)$ of $Yb_3Co_4Ge_{13}$ drops down almost to zero. In the whole studied temperature range the thermal conductivity is very low and comparable with such famous thermoelectric materials as filled skutterudites[3] or clathrates.[51] Since no enlarged voids are observed in the crystal structure of $Yb_3Co_4Ge_{13}$ and thus, no signs of any rattling effects, we ascribe this low $\kappa(T)$ to the strong crystallographic disorder in the studied germanide. By applying the Wiedemann-Franz law we decomposed

$\kappa(T)$ of $Yb_3Co_4Ge_{13}$ in electronic [$\kappa_{el}(T) = L_0T/\rho(T)$, where $L_0 = 2.44 \times 10^{-8}\,\mathrm{W\,\Omega\,K^{-2}}$ is the Lorenz number] and phononic [$\kappa_{ph}(T) = \kappa(T) - \kappa_{el}(T)$] parts. Interestingly, as one can see from Fig. 10, $\kappa(T)$ is dominated by phononic contributions for $T < 200\,\mathrm{K}$ (*i.e.* in the IV regime), whereas above this temperatures (*i.e.* Yb^{3+} regime) electrons are responsible for the heat transport. Phonon-mediated thermal conductivity is a common feature of many IV systems (*e.g.* $YbPtGe_2$,[40] $CePd_3$,[52] CeNiSn[53] *etc.*).

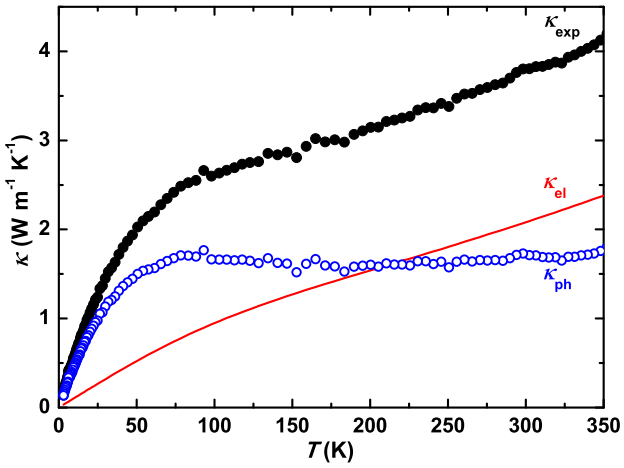

Figure 10: Temperature dependence of the thermal conductivity with its phononic and electronic parts for $Yb_3Co_4Ge_{13}$.

Conclusions

From refinement of single crystal and powder X-ray diffraction (XRD) data $Yb_3Co_4Ge_{13}$ is found to crystallize with a $3D + 3$ modulated structure. Powder XRD as well as a high-resolution transmission electron microscopy (HRTEM) study indicated the cubic body-centered (space group $I4_132$, $a \approx 17.5\,\mathrm{\AA}$) $La_3Rh_4Sn_{13}$ type to be an averaged structure of the modulated one. Off-stoichiometric $Yb_{3.2}Co_4Ge_{12.8}$ is found to crystallize with the primitive cubic (space group $Pm\bar{3}n$, $a \approx 8.7\,\mathrm{\AA}$) $Yb_3Rh_4Sn_{13}$ Remeika prototype however, with a strong structural disorder.

X-ray absorption spectroscopy (XAS) revealed the valence of Yb-ions in the structure of $Yb_3Co_4Ge_{13}$ to be temperature dependent and to vary within $+2.60 - +2.66$ for $85\,\mathrm{K} < T <$

293 K. In agreement with this finding, a broad and well pronounced maximum is observed in the magnetic susceptibility. It can be analysed by interconfiguration fluctuation- as well as by Coqblin-Schrieffer models. However, the first one resulted in much lower Yb-valences for $T < 250$ K than those obtained from XAS, while the latter one indicated $J = 5/2$ instead of the expected $J = 7/2$ whole multiplet for Yb^{3+}-ions. Probably, the crystal electric field splitting is strongly contributing to the low temperature physics of $Yb_3Co_4Ge_{13}$.

Measurements of electrical and thermal transport properties indicated $Yb_3Co_4Ge_{13}$ to be a metal. The Kadowaki-Woods ratio deduced from specific heat and electrical resistivity is close to this expected for Yb-based intermediate valence (IV) systems. In agreement with this observation the temperature dependence of the Seebeck coefficient $S(T)$ reveals a maximum, which can be fairly reproduced by a phenomenological model. $S(T)$ is also positive in the whole studied temperature range and implies holes as charge carriers in $Yb_3Co_4Ge_{13}$. The thermal conductivity of the studied germanide is relatively low and dominated by the phononic contribution as it is the case for a number of IV systems.

Acknowledgement

This work was performed within the Deutsche Forschungsgemeinschaft (DFG) grant 325295543. The authors thank H. Borrmann, A.A. Tsirlin and C. Hennig for performing XRD measurements. The authors are also grateful to U. Burkhardt, S. Kostmann and P. Scheppan for microstructural and EDX studies as well as to Y. Grin and E. Kroke for their interest in this work.

References

(1) Carrillo-Cabrera, W.; Cardoso Gil, R.; Paschen, S.; Grin, Y. Crystal structure of $Ba_8Ga_{4.44}Ge_{39.14}\square_{2.42}$, $Ba_8Ga_{8.62}Ge_{36}\square_{1.38}$, and $Ba_8Ga_{12.35}Ge_{33.27}\square_{0.38}$, three clathrate-I variants. *Z. Kristallogr. NCS* **2002**, *217*, 183–185.

(2) Zhang, H.; Borrmann, H.; Oeschler, N.; Candolfi, C.; Schnelle, W.; Schmidt, M.; Burkhardt, U.; Baitinger, M.; Zhao, J.-T.; Grin, Y. Atomic Interactions in the p-Type Clathrate I $Ba_8Au_{5.3}Ge_{40.7}$. *Inorg. Chem.* **2011**, *50*, 1250–1257.

(3) Uher, C. In *Recent Trends in Thermoelectric Materials Research I*; Tritt, T. M., Ed.; Semiconductors and Semimetals; Elsevier, 2001; Vol. 69; pp 139 – 253.

(4) Remeika, J.; Espinosa, G.; Cooper, A.; Barz, H.; Rowell, J.; McWhan, D.; Vandenberg, J.; Moncton, D.; Fisk, Z.; Woolf, L.; Hamaker, H.; Maple, M.; Shirane, G.; Thomlinson, W. A new family of ternary intermetallic superconducting/magnetic stannides. *Solid State Commun.* **1980**, *34*, 923 – 926.

(5) Gumeniuk, R. In *Handbook on the Physics and Chemistry of Rare Earths*; Bünzli, J.-C. G., Pecharsky, V. K., Eds.; Structural and Physical Properties of Remeika Phases; Elsevier, 2018; Vol. 54; pp 43 – 143.

(6) Varma, C. M. Mixed-valence compounds. *Rev. Mod. Phys.* **1976**, *48*, 219–238.

(7) Lawrence, J. M.; Riseborough, P. S.; Parks, R. D. Valence fluctuation phenomena. *Rep. Prog. Phys.* **1981**, *44*, 1–84.

(8) Sales, B. C.; Wohlleben, D. K. Susceptibility of Interconfiguration-Fluctuation Compounds. *Phys. Rev. Lett.* **1975**, *35*, 1240–1244.

(9) Rajan, V. T. Magnetic Susceptibility and Specific Heat of the Coqblin-Schrieffer Model. *Phys. Rev. Lett.* **1983**, *51*, 308–311.

(10) Bickers, N. E.; Cox, D. L.; Wilkins, J. W. Self-consistent large-N expansion for normal-state properties of dilute magnetic alloys. *Phys. Rev. B* **1987**, *36*, 2036–2079.

(11) Schlottmann, P. Some exact results for dilute mixed-valent and heavy-fermion systems. *Phys. Rep.* **1989**, *181*, 1 – 119.

(12) Hewson, A.; Rasul, J.; Newns, D. Magnetic isotherm for YbCuAl — Comparison with exact results for the Coqblin-Schrieffer model. *Solid State Commun.* **1983**, *47*, 59 – 61.

(13) Kasaya, M.; Iga, F.; Takigawa, M.; Kasuya, T. Mixed valence properties of YbB12. *J. Magn. Magn. Mater.* **1985**, *47-48*, 429 – 435.

(14) Mudryk, Y.; Grytsiv, A.; Rogl, P.; Dusek, C.; Galatanu, A.; Idl, E.; Michor, H.; Bauer, E.; Godart, C.; Kaczorowski, D.; Romaka, L.; Bodak, O. Physical properties and superconductivity of skutterudite-related $Yb_3Co_{4.3}Sn_{12.7}$ and $Yb_3Co_4Ge_{13}$. *J. Phys. Condens. Matter* **2001**, *13*, 7391–7402.

(15) Rai, B. K.; Oswald, I. W. H.; Chan, J. Y.; Morosan, E. Intermediate valence to heavy fermion through a quantum phase transition in $Yb_3Rh_{1-x}T_x)_4Ge_{13}$ ($T = \mathrm{Co}, \mathrm{Ir}$) single crystals. *Phys. Rev. B* **2016**, *93*, 035101.

(16) Morozkin, A.; Irkhin, V.; Nikiforov, V. Thermoelectric properties of $Pr_3Rh_4Sn_{13}$-type $Yb_3Co_4Ge_{13}$ and $Yb_3Co_4Sn_{13}$ compounds. *J. Alloys Compd.* **2013**, *549*, 121 – 125.

(17) Bordet, P.; Cox, D.; Espinosa, G.; Hodeau, J.; Marezio, M. Synchrotron X-ray powder diffraction study of the phase I' compound: $SnLa_3Rh_4Sn_{12}$. *Solid State Commun.* **1991**, *78*, 359 – 366.

(18) Gumeniuk, R.; Akselrud, L.; Kvashnina, K. O.; Schnelle, W.; Tsirlin, A. A.; Curfs, C.; Rosner, H.; Schöneich, M.; Burkhardt, U.; Schwarz, U.; Grin, Y.; Leithe-Jasper, A. $Ca_3Pt_{4+x}Ge_{13-y}$ and $Yb_3Pt_4Ge_{13}$: new derivatives of the $Pr_3Rh_4Sn_{13}$ structure type. *Dalton Trans.* **2012**, *41*, 6299–6309.

(19) Gumeniuk, R.; Nicklas, M.; Akselrud, L.; Schnelle, W.; Schwarz, U.; Tsirlin, A. A.; Leithe-Jasper, A.; Grin, Y. $Y_3Pt_4Ge_{13}$: A superconductor with a noncentrosymmetric crystal structure. *Phys. Rev. B* **2013**, *87*, 224502.

(20) Gumeniuk, R.; Schöneich, M.; Kvashnina, K. O.; Akselrud, L.; Tsirlin, A. A.; Nicklas, M.; Schnelle, W.; Janson, O.; Zheng, Q.; Curfs, C.; Burkhardt, U.; Schwarz, U.; Leithe-Jasper, A. Intermetallic germanides with non-centrosymmetric structures derived from the $Yb_3Rh_4Sn_{13}$ type. *Dalton Trans.* **2015**, *44*, 5638–5651.

(21) Akselrud, L.; Grin, Y. WinCSD: software package for crystallographic calculations (Version 4). *J. Appl. Crystallogr.* **2014**, *47*, 803–805.

(22) MacTampas, Total Resolution LLC.

(23) P. Stadelmann: JEMS - Electron Microscopy Software, Java version, CIME - EPFÖ Switzerland, 1999 − 2011.

(24) Pinheiro, C. B.; Abakumov, A. M. Superspace crystallography: a key to the chemistry and properties. *IUCrJ* **2015**, *2*, 137–154.

(25) Stokes, H. T.; Campbell, B. J.; van Smaalen, S. Generation of $(3 + d)$-dimensional superspace groups for describing the symmetry of modulated crystalline structures. *Acta Crystallogr. A* **2011**, *67*, 45–55.

(26) van Smaalen, S.; Campbell, B. J.; Stokes, H. T. Equivalence of superspace groups. *Acta Crystallogr. A* **2013**, *69*, 75–90.

(27) Petříček, V.; Van Der Lee, A.; Evain, M. On the use of crenel functions for occupationally modulated structures. *Acta Cryst. A* **1995**, *51*, 529–535.

(28) Withers, R. L.; Ling, C. D.; Schmid, S. Atomic Modulation Functions, Periodic Nodal Surfaces and the three-dimensional incommensurately modulated $(1 - x)Bi_2O_3 \cdot xNb_2O_5$, $0.06 < x < 0.23$, solid solution. *Z. Kristallogr.* **1999**, *214*, 296–304.

(29) Wagner, T.; Schönleber, A. A non-mathematical introduction to the superspace description of modulated structures. *Acta Cryst. B* **2009**, *65*, 249–268.

(30) Levytskyi, V.; Feig, M.; Akselrud, L.; Schnelle, W.; Leithe-Jasper, A.; Dyadkin, V.; Chernyshov, D.; Gumeniuk, R. Crystal structure and superconducting properties of $Sc_5Ir_6Sn_{18}$. *J. Phys. Condens. Matter* **2019**, *31*, 445603.

(31) Feig, M.; Akselrud, L.; Schnelle, W.; Dyadkin, V.; Chernyshov, D.; Ormeci, A.; Simon, P.; Leithe-Jasper, A.; Gumeniuk, R. Crystal structure, chemical bonding, and electrical and thermal transport in $Sc_5Rh_6Sn_{18}$. *Dalton Trans.* **2020**, *49*, 6832–6841.

(32) Emsley, J. *The Elements*; Clarendon Press: Oxford, 1998.

(33) Buschow, K. H. J.; Goebel, U.; Dormann, E. Valence Instabilities in $CeSn_3$ and $YbAl_3$. *Phys. Status Solidi B* **1979**, *93*, 607–615.

(34) Kasaya, M.; Iga, F.; Negishi, K.; Nakai, S.; Kasuya, T. A new and typical valence fluctuating system, YbB_{12}. *J. Magn. Magn. Mater.* **1983**, *31-34*, 437 – 438.

(35) Paramanik, U.; Anupam,; Burkhardt, U.; Prasad, R.; Geibel, C.; Hossain, Z. Valence fluctuation in $CeMo_2Si_2C$. *J. Alloys Compd.* **2013**, *580*, 435 – 441.

(36) Gamża, M. B.; Gumeniuk, R.; Burkhardt, U.; Schnelle, W.; Rosner, H.; Leithe-Jasper, A.; Ślebarski, A. Coexistence of magnetic order and valence fluctuations in the Kondo lattice system $Ce_2Rh_3Sn_5$. *Phys. Rev. B* **2017**, *95*, 165142.

(37) Gumeniuk, R.; Schnelle, W.; Ahmida, M. A.; Abd-Elmeguid, M. M.; Kvashnina, K. O.; Tsirlin, A. A.; Leithe-Jasper, A.; Geibel, C. Valence fluctuations of europium in the boride $Eu_4Pd_{29+x}B_8$. *J. Phys. Condens. Matter* **2016**, *28*, 115601.

(38) Seiro, S.; Kummer, K.; Vyalikh, D.; Caroca-Canales, N.; Geibel, C. Anomalous susceptibility in single crystals of $EuCo_2Si_2$ with trivalent Eu: Influence of excited J multiplets. *Phys. status solidi (b)* **2013**, *250*, 621–625.

(39) Seiro, S.; Prots, Y.; Kummer, K.; Rosner, H.; Gil, R. C.; Geibel, C. Charge, lattice

and magnetism across the valence crossover in $EuIr_2Si_2$ single crystals. *J. Phys.: Cond. Matter* **2019**, *31*, 305602.

(40) Gumeniuk, R.; Sarkar, R.; Geibel, C.; Schnelle, W.; Paulmann, C.; Baenitz, M.; Tsirlin, A. A.; Guritanu, V.; Sichelschmidt, J.; Grin, Y.; Leithe-Jasper, A. $YbPtGe_2$: A multivalent charge-ordered system with an unusual spin pseudogap. *Phys. Rev. B* **2012**, *86*, 235138.

(41) Jiang, W. B. et al. Crossover from a heavy fermion to intermediate valence state in noncentrosymmetric $Yb_2Ni_{12}(P,As)_7$. *Sci. Rep.* **2015**, *5*, 17608.

(42) Rasul, J. W.; Hewson, A. C. Bethe ansatz and 1/N expansion results for N-fold degenerate magnetic impurity models. *J. Phys. C: Solid State Phys.* **1984**, *17*, 2555–2573.

(43) Yamaoka, H.; Tsujii, N.; Utsumi, Y.; Sato, H.; Jarrige, I.; Yamamoto, Y.; Lin, J.-F.; Hiraoka, N.; Ishii, H.; Tsuei, K.-D.; Mizuki, J. Valence transitions in the heavy-fermion compound YbCuAl as a function of temperature and pressure. *Phys. Rev. B* **2013**, *87*, 205120.

(44) Michor, H.; Kreiner, K.; Tsujii, N.; Yoshimura, K.; Kosuge, K.; Hilscher, G. Crystalline electric field and Kondo energy scales in $YbCu_{5-x}Ag_x$. *Phys. B: Cond. Matter* **2002**, *319*, 277–281.

(45) Rundqvist, S.; Jellinek, F. The Structures of Ni_6Si_2B, Fe_2P and Related Phases. *Acta Chem. Scand.* **1959**, *13*, 425–432.

(46) Haucke, W. Kristallstruktur von $CaZn_5$ und $CaCu_5$. *Z. Anorg. Allg. Chem.* **1940**, *244*, 17–22.

(47) Moon, R. M.; Child, H. R.; Koehler, W. C.; Raubenheimer, L. J. Magnetic Structure of Er_2O_3 and Yb_2O_3. *J. Appl. Phys.* **1967**, *38*, 1383–1383.

(48) Kadowaki, K.; Woods, S. Universal relationship of the resistivity and specific heat in heavy-Fermion compounds. *Solid State Commun.* **1986**, *58*, 507 – 509.

(49) Tsujii, N.; Yoshimura, K.; Kosuge, K. Deviation from the Kadowaki Woods relation in Yb-based intermediate-valence systems. *J. Phys. Condens. Matter* **2003**, *15*, 1993–2003.

(50) Gottwick, U.; Gloss, K.; Horn, S.; Steglich, F.; Grewe, N. Transport coefficients of intermediate valent $CeNi_x$ intermetallic compounds. *J. Magn. Magn. Mater.* **1985**, *47-48*, 536 – 538.

(51) Cohn, J. L.; Nolas, G. S.; Fessatidis, V.; Metcalf, T. H.; Slack, G. A. Glasslike Heat Conduction in High-Mobility Crystalline Semiconductors. *Phys. Rev. Lett.* **1999**, *82*, 779–782.

(52) Gumeniuk, R.; Schnelle, W.; Kvashnina, K. O.; Leithe-Jasper, A. Kondo effect and thermoelectric transport in $CePd_3Be_x$. *J. Phys. Condens. Matter* **2016**, *28*, 165603.

(53) Aliev, F. G.; Villar, R.; Vieira, S.; Lopez de la Torre, M. A.; Scolozdra, R. V.; Maple, M. B. Energy gap of the ground state of CeNiSn caused by local and long-range magnetic-moment interactions. *Phys. Rev. B* **1993**, *47*, 769–772.

Supporting Information

Table S1: Atomic coordinates, occupational and displacement parameters in $Yb_{3+x}Co_4Ge_{13-x}$ ($x = 0, 0.2$)

Atom	Site	G	Atomic coordinates			B_{eq}
			x	y	z	
$Yb_3Co_4Ge_{13}$ (modulated)						
Yb	6*d*	0.976(1)	0	1/4	1/2	0.690(4)
Co	8*e*		0.2488(1)	x	x	0.785(6)
Ge1	2*a*		0	0	0	0.36(1)
Ge2	24*i*	0.640(1)	0.32378(6)	0.16007(6)	0.0018(1)	0.31(1)
Ge3	24*i*	0.363(3)	0.2765(1)	0.1420(1)	0.0008(2)	0.30(4)
$Yb_3Co_4Ge_{13}$ (approximant)						
Yb1	24*g*		1/8	0.2495(9)	$y + 1/4$	0.26(9)
Yb2	24*h*		1/8	0.2495(6)	$-y + 1/4$	0.45(8)
Co1	8*a*		1/8	1/8	1/8	0.93(8)
Co2	8*b*		7/8	7/8	7/8	0.92(9)
Co3	24*g*		1/8	0.124(2)	$y + 1/4$	0.78(9)
Co4	24*h*		1/8	0.622(2)	$-y + 1/4$	0.78(5)
Ge1	16*e*		0.001(1)	x	x	0.82(5)
Ge2	48*i*		0.0881(1)	0.250(1)	0.332(2)	0.88(9)
Ge3	48*i*		0.251(1)	0.327(2)	0.407(1)	0.83(9)
Ge4	48*i*		0.001(1)	0.157(1)	0.079(2)	0.97(9)
Ge5	48*i*		0.177(2)	0.389(1)	0.251(2)	0.94(5)
$Yb_{3.2}Co_4Ge_{12.8}$						
Yb1	6*c*		1/4	0	1/2	0.51(9)
Yb2	2*a*	0.21(1)	0	0	0	0.86(8)
Co	8*e*		1/4	1/4	1/4	0.32(7)
Ge1	16*i*	0.10(1)	0.019(2)	x	x	1.0(2)
Ge2	24*k*	0.27(1)	0	0.1431(2)	0.2738(2)	0.68(2)
Ge2a	24*k*	0.73(1)	0	0.1593(2)	0.3211(2)	0.66(2)

Table S2: Modulation amplitudes of the displacive modulation in $Yb_3Co_4Ge_{13}$.

Atom	$F^{(i)}_{xyz}$	U_{cryst}	U_{powder}	Atom	$F^{(i)}_{xyz}$	U_{cryst}	U_{powder}
Yb	$F^{(1)}_{z}$	0.0143(1)	-0.0017(5)	Ge2	$F^{(23)}_{x}$	0.0110(2)	-0.0052(9)
	$F^{(2)}_{y}$	0.0066(1)	-0.0029(2)		$F^{(23)}_{y}$	-0.00136(2)	0.000(1)
	$F^{(3)}_{xz}$	0.0064(1)	-0.0003(4)		$F^{(23)}_{z}$	-0.0093(3)	-0.003(1)
	$F^{(4)}_{xz}$	0.0069(1)	0.0004(2)		$F^{(21)}_{x}$	0.0127(2)	0.0018(8)
	$F^{(5)}_{y}$	-0.0043(1)	0.0007(3)		$F^{(21)}_{y}$	0.0075(2)	0.0037(9)
	$F^{(6)}_{xz}$	0.0079(1)	-0.0016(3)		$F^{(21)}_{z}$	0.0108(2)	0.000(1)
	$F^{(7)}_{y}$	0.0097(1)	0.0039(2)		$F^{(24)}_{x}$	0.0064(2)	-0.0158(5)
	$F^{(8)}_{xz}$	-0.0023(2)	-0.0006(4)		$F^{(24)}_{y}$	0.0099(2)	-0.0068(6)
	$F^{(9)}_{xz}$	0.0074(1)	-0.0008(4)		$F^{(24)}_{z}$	0.0050(3)	0.0085(9)
Co	$\mathrm{F}^{(10)}_{\mathrm{xyz}}$	-0.0003(3)	-0.0004(6)	Ge3	$\mathrm{F}^{(19)}_{\mathrm{x}}$	0.0105(4)	-0.005(1)
	$F^{(11)}_{xyz}$	0.0065(2)	0.0070(5)		$F^{(19)}_{y}$	-0.0060(4)	0.000(1)
	$F^{(12)}_{xyz}$	-0.0139(1)	0.0023(5)		$F^{(19)}_{z}$	-0.0112(3)	0.002(2)
	$F^{(13)}_{xyz}$	0.0034(2)	-0.0037(8)		$F^{(22)}_{x}$	0.0075(3)	-0.011(1)
	$F^{(14)}_{xyz}$	0.0135(1)	-0.0036(7)		$F^{(22)}_{y}$	0.0238(2)	-0.001(2)
	$F^{(15)}_{xyz}$	-0.0018(2)	0.0026(8)		$F^{(22)}_{z}$	-0.0184(3)	-0.004(2)
Ge1	$F^{(16)}_{\mathrm{z}}$	0.0106(4)	0.0172(7)		$F^{(20)}_{\mathrm{x}}$	0.0146(3)	0.017(1)
	$F^{(17)}_{xyz}$	0.0171(1)	0.0021(7)		$F^{(20)}_{y}$	-0.0062(4)	0.004(1)
	$F^{(18)}_{xyz}$	-0.0059(2)	-0.0027(7)		$F^{(20)}_{z}$	0.0154(3)	0.005(2)
Ge2	$\mathrm{F}^{(19)}_{\mathrm{x}}$	-0.0055(2)	0.0029(6)		$\mathrm{F}^{(23)}_{\mathrm{x}}$	-0.0109(4)	-0.001(2)
	$F^{(19)}_{y}$	0.0173(2)	-0.0049(6)		$F^{(23)}_{y}$	0.0063(4)	0.005(2)
	$F^{(19)}_{z}$	0.0088(2)	-0.0044(7)		$F^{(23)}_{z}$	0.0057(5)	0.002(2)
	$F^{(22)}_{x}$	-0.0093(3)	-0.0043(9)		$F^{(21)}_{x}$	-0.0070(3)	-0.001(1)
	$F^{(22)}_{y}$	-0.0042(3)	-0.003(1)		$F^{(21)}_{y}$	-0.0091(3)	0.003(1)
	$F^{(22)}_{z}$	0.0076(3)	0.0002(8)		$F^{(21)}_{z}$	-0.0006(4)	0.003(2)
	$F^{(20)}_{x}$	0.0213(2)	-0.0069(8)		$F^{(24)}_{x}$	0.0198(3)	-0.0166(8)
	$F^{(20)}_{y}$	0.0061(2)	-0.004(1)		$F^{(24)}_{y}$	0.0006(4)	-0.0045(9)
	$F^{(20)}_{z}$	-0.0104(2)	-0.0019(9)		$F^{(24)}_{z}$	-0.0020(5)	-0.004(2)

Table S3: Occupational modulation amplitudes in $Yb_3Co_4Ge_{13}$.*

Atom	F_{xyz}	U_{cryst}	U_{powder}	Atom	F_{xyz}	U_{mono}	U_{Powder}
Ge2	$F^{(19)}$	0.043(3)	-0.148(7)	Ge3	$F^{(19)}$	-0.111(1)	0.167(8)
	$F^{(20)}$	-0.089(2)	-0.035(8)		$F^{(20)}$	0.006(1)	-0.007(7)
	$F^{(21)}$	-0.054(3)	0.15(1)		$F^{(21)}$	-0.260(1)	-0.14(1)
	$F^{(22)}$	0.089(3)	0.12(1)		$F^{(22)}$	-0.099(1)	-0.13(1)
	$F^{(23)}$	0.103(3)	0.04(1)		$F^{(23)}$	-0.001(1)	0.00(1)
	$F^{(24)}$	0.147(3)	0.081(6)		$F^{(24)}$	-0.007(2)	-0.146(7)

*Modulation functions for *sin* and *cos* of Fourier terms: $p = p_0 + \sum_i U^i F^i(x_4, x_5, x_6)_p$

$x = x_0 + \sum_i U^i F^i(x_4, x_5, x_6)_x$;
$y = y_0 + \sum_i U^i F^i(x_4, x_5, x_6)_y$;
$z = z_0 + \sum_i U^i F^i(x_4, x_5, x_6)_z$;

$F^{(1)} = [cos(x_5 - x_6) - cos(x_5 + x_6)]_z$
$F^{(2)} = [cos(x_4 + x_5) + cos(x_4 - x_5) - cos(x_5 - x_6) - cos(x_5 + x_6)]_y$
$F^{(3)} = [cos(x_5 + x_6) - cos(x_5 - x_6)]_x + [cos(x_4 + x_5) - cos(x_4 - x_5)]_z$
$F^{(4)} = [sin(x_4 + x_5) + sin(x_4 - x_5)]_x + [sin(x_5 + x_6) - sin(x_5 - x_6)]_z$
$F^{(5)} = [sin(x_4 + x_5) - sin(x_4 - x_5) + sin(x_5 - x_6) + sin(x_5 + x_6)]_y$
$F^{(6)} = [sin(x_5 - x_6) - sin(x_5 + x_6)]_x + [sin(x_4 + x_5) + sin(x_4 - x_5)]_z$
$F^{(7)} = [cos(x_4 + x_6) - cos(x_4 - x_6)]_y$
$F^{(8)} = [sin(x_4 + x_6)]_x - [sin(x_4 - x_6)]_z$
$F^{(9)} = [sin(x_4 - x_6)]_x + [sin(x_4 + x_6)]_z$

$F^{(10)} = [cos(x_4 + x_5)]_x + [cos(x_5 + x_6)]_y + [cos(x_4 + x_6)]_z$
$F^{(11)} = [cos(x_4 + x_6)]_x + [cos(x_4 + x_5)]_y + [cos(x_5 + x_6)]_z$
$F^{(12)} = [cos(x_5 + x_6)]_x + [cos(x_4 + x_6)]_y + [cos(x_4 + x_5)]_z$
$F^{(13)} = [sin(x_4 + x_5)]_x + [sin(x_5 + x_6)]_y + [sin(x_4 + x_6)]_z$
$F^{(14)} = [sin(x_4 + x_6)]_x + [sin(x_4 + x_5)]_y + [cos(x_5 + x_6)]_z$
$F^{(15)} = [sin(x_5 + x_6)]_x + [sin(x_4 + x_6)]_y + [sin(x_4 + x_5)]_z$

$F^{(16)} = [cos(x_4 + x_5) - cos(x_4 - x_5)]_z$
$F^{(17)} = [sin(x_4{+}x_5){+}sin(x_4{-}x_5)]_x{+}[sin(x_5{+}x_6){+}sin(x_5{-}x_6)]_y{+}[sin(x_4{+}x_6){-}sin(x_4{-}x_6)]_z$
$F^{(18)} = [sin(x_4{+}x_6){+}sin(x_4{-}x_6)]_x{+}[sin(x_4{+}x_5){-}sin(x_4{-}x_5)]_y{+}[sin(x_5{+}x_6){-}sin(x_5{-}x_6)]_z$

$F^{(19)} = [cos(x_4 + x_5)]$
$F^{(20)} = [cos(x_4 + x_6)]$
$F^{(21)} = [cos(x_5 + x_6)]$
$F^{(22)} = [sin(x_4 + x_5)]$
$F^{(23)} = [sin(x_4 + x_6)]$
$F^{(24)} = [sin(x_5 + x_6)]$

Table S4: Anisotropic parameters for the modulated $Yb_3Co_4Ge_{13}$

Atom	B_{11}	B_{22}	B_{33}	B_{12}	B_{13}	B_{23}
Yb	0.532(6)	1.01(1)	B11	0	0	0
Co	0.79(1)	B11	B11	0.140(6)	B12	B12
Ge1	0.36(2)	B11	B11	0	0	0
Ge2	0.17(2)	0.15(2)	0.61(2)	0.022(8)	0.02(2)	0.02(2)
Ge3	0.44(7)	0.25(6)	0.21(6)	0.07(3)	-0.18(4)	0.15(4)

Table S5: Interatomic distances (Å) in $Yb_{3+x}Co_4Ge_{13-x}$ ($x = 0, 0.2$)

Contact	$Yb_3Co_4Ge_{13}$ ($I4_132$)	$Yb_{3.2}Co_4Ge_{12.8}$ ($Pm\bar{3}n$)
Yb-Ge	2.990(2) – 3.186(3)	3.026(1) – 3.201(1)
Yb-Co	3.047(3) – 3.170(3)	3.0903(1) – 3.7848(1)
Yb-Yb	4.3613(1)	4.3704(1)
Co-Ge	2.355(4) – 2.430(4)	2.3856(6) – 3.499(2)
Co-Co		> 4.3 Å
Ge-Ge	2.630(2) – 3.412(4)	2.484(2) – 3.359(2)

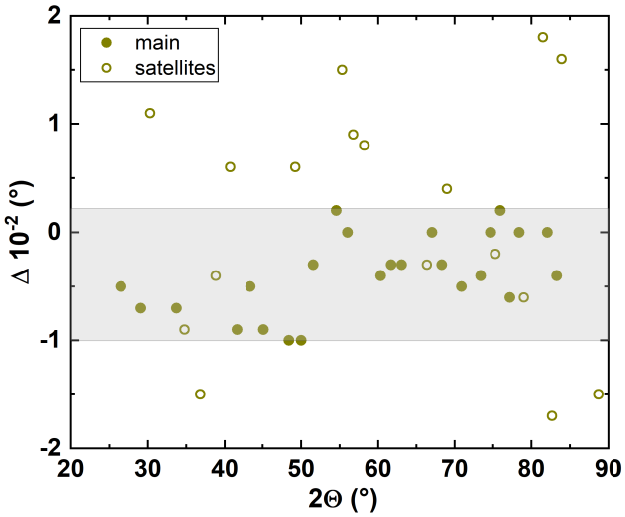

Figure S1: Dependence of the systematic deviations Δ of reflections' indexing *vs.* 2Θ for $Yb_3Co_4Ge_{13}$.